Article

Not peer-reviewed version

Composite Photocatalysts with Fe, Co, Ni Oxides on Supports with Tetracoordinated Ti Embedded into Aluminosilicate Gel during Zeolite Y Synthesis

Gabriela Petcu * , Elena Maria Anghel , Irina Atkinson , Daniela C. Culita , Nicoleta G. Apostol , Andrei Kuncser , Florica Papa , Adriana Băran , Jean-Luc Blin , Viorica Parvulescu *

Posted Date: 7 December 2023

doi: 10.20944/preprints202312.0455.v1

Keywords: Ti-aluminosilicate gel; Ti-zeolite Y; Fe, Co, Ni/Ti-zeolite Y; Co oxides; cefuroxime degradation; photocatalysis; scavenger experiments.

doi:10.20944/preprints202312.0455.v1

Article

Composite Photocatalysts with Fe, Co, Ni Oxides on Supports with Tetracoordinated Ti Embedded into Aluminosilicate Gel During Zeolite Y Synthesis

Gabriela Petcu [1,*], Elena M. Anghel [1], Irina Atkinson [1], Daniela C. Culita [1], Nicoleta G. Apostol [2], Andrei Kuncser [2], Florica Papa [1], Adriana Baran [1], Jean-Luc Blin [3] and Viorica Parvulescu [1,*]

[1] Institute of Physical Chemistry "Ilie Murgulescu" of the Romanian Academy, 202 Splaiul Independentei, 060021 Bucharest, Romania; gpetcu@icf.ro (G.P.), manghel@icf.ro (E.M.A.), iatkinson@icf.ro (I.A.), dculita@icf.ro (D.C.C.), floricapapa@gmail.com (F.P.), adibaran@gmail.com (A.B.), vpirvulescu@icf.ro (V.P.)

[2] National Institute of Materials Physics, Atomistilor 405A, 077125 Magurele, Romania; nicoleta.apostol@infim.ro; andrei.kuncser@infim.ro

[3] Faculty of Sciences and Technology, University of Lorraine, CNRS, L2CM, F-54000 Nancy, France; jean-luc.blin@univ-lorraine.fr

* Correspondence: gpetcu@icf.ro (G.P.), vpirvulescu@icf.ro (V.P.)

Abstract: Ti - aluminosilicate gels were used as supports for immobilization of Fe, Co and Ni oxides (5%) by impregnation, and synthesis of efficient photocatalysts for degradation of β-lactam antibiotic from water. Titanium oxide (1 and 2%) was incorporated into the zeolite network by modifying the gel during the zeolitization process. The formation of the zeolite Y structure and its microporous structure were evidenced by X-ray diffraction and N_2 physisorption. The structure, composition, reduction and optical properties were studied by X-ray diffraction, H_2-TPR, XPS, Raman, photoluminiscence and UV-Vis spectroscopy. The obtained results indicated a zeolite Y structure for all photocatalysts with tetracoordinated Ti^{4+} sites. The immobilized metals from group VIII are both in the form of metal oxides such as Fe_2O_3, Fe_3O_4, CoO, Co_3O_4, NiO and also in the metallic state (Fe^0, Co^0, and Ni^0). A red shift of the absorption edge was observed in UV - Vis spectra of photocatalysts upon addition of Fe, Co or Ni species. The photocatalytic performances were evaluated in degradation of cefuroxime from water under visible light irradiation. The best results were obtained for iron immobilized photocatalysts. Scavenger experiments explained the photocatalytic results and their mechanisms. A different contribution of the active species to the photocatalytic reactions was evidenced.

Keywords: Ti-aluminosilicate gel; Ti-zeolite Y; Fe; Co; Ni/Ti-zeolite Y; cefuroxime degradation; photocatalysis; scavenger experiments

1. Introduction

Zeolites are support materials widely used for hybrid adsorbents and photocatalyst applications [1-7] due to their adjustable properties such as high surface area, adsorption, environmentally friendly nature, hydrophobe/hydrophilic surface, and abundant acid/base sites. In photocatalytic reactions, the zeolite acts as a host for the semiconductors or other photoactive guests, and acid/base sites can reduce the electron and hole recombination [1]. In addition, to improve the separation of photogenerated charge carriers, the zeolite was doped with metal/non-metal or by introducing other semiconductors with a narrow band gap. The most used zeolites are zeolite Y [4,8,9], zeolite 5A [1, 3, 10, 11] and natural zeolites [12, 13]. The previous results [1, 14, 15] reported that the efficiency of TiO_2/zeolite photocatalysts was optimized by an adequate choice of the zeolite type with a certain Si/Al molar ratio, specific surface area, and hydrophobicity. Also, among isolated metal oxide moieties with tetrahedral coordination geometry embedded in heteroatom-containing zeolites, titanium oxide has attracted considerable attention. The photocatalytic activity and selectivity of tetra-coordinated Ti^{4+} species from framework of titanium silicalite-1 (TS-1), which is the most representative one of the "single-site heterogeneous catalysts" is much higher than that of octahedrally coordinated Ti in TiO_2 semiconductor [16]. The mechanism proposed for the photocatalytic reactions is based on the ligand-to-metal charge transfer (LMCT) process (Ti^{4+}- O^{2-} $\xrightarrow{h\nu}$ Ti^{3+}- O^{-}). However, TS-1 based photocatalysts are relatively less developed and the largest limitation is the content of the framework Ti. Much of the relevant research was focused on zeolite synthesis with higher tetra-coordinated Ti in the framework [17, 18]. Mesoporous TS-1 with high Ti active site (Ti/(Si+ Ti) > 5%) has been successfully synthesized by using the combined (sol-gel/dry gel conversion) method [18]. Thus, the first step was obtained by sol-gel method amorphous SiO_2-TiO_2 solids with Si-O-Ti bonds. These mixed oxides were impregnated with TPAOH solution and hydrothermally treated to obtain more Ti in TS-1.

The first studies regarding the introduction of titanium into the zeolite Y network by direct synthesis and the effect of Ti concentration on the zeolite structure were carried out by our group [19, 20]. Zeolite Y is a faujasite molecular sieve with 7.35 Å diameter pores and a three-dimensional pore structure. The basic structural units are sodalite cages that form supercages that host spheres with high diameters (11.24 Å) [1]. The preservation of the zeolitic network was obtained for 1 and 2% TiO_2 and its partial disruption for 5% TiO_2. The synthesis of Ti-Y and the effect of titanium concentration on the formation of zeolite Y structure were evaluated by freezing the sol-gel phases at various periods [20].

In the photocatalytic reactions, Ti sites possess strong adsorption capacity for the activated reactant molecules and the coordinated O sites can accept reaction intermediates. Since the TiO_2/zeolite composites exhibit high photocatalytic activity only under UV light irradiation, many approaches have sought to expand the field of applicability of these photocatalysts to visible light by doping of a small amount of noble and transition metals [21-27]. A special interest was evidenced in noble metal nanoparticles (Pt, Pd, Au, Ag) because of their plasmonic properties [8, 9, 28, 29]. The combination of noble metals with another cheaper and more abundant transition metal was also studied [24]. Among the transition metals whose ions are capable of modifying the optoelectronics properties of TiO_2, the following stood out: V, Cr, Fe, Co, Ni, Cu, and Zn [21-23, 25-27]. The immobilization of these metals on TiO_2/zeolite created active species, modified the surface properties and also promoted the photoinduced carrier separation, and consequently enhanced the photocatalytic activity. The photocatalytic degradation mechanism on zeolite-based photocatalysts can vary for different organic compounds due to their sensitization effect. For instance, our previous results evidenced the high activity of Co–Ti- or Ni–Ti-supported photocatalysts on zeolite Y, with microporous and hierarchical structures, in amoxicillin photodegradation [30]. The degradation mechanism of amoxicillin (β-lactam antibiotic) under UV and visible light irradiation, investigated in the presence of scavengers, evidenced the effect of metal species interaction and zeolite support. Hence, for practical environmental applications the zeolite properties, supported metals, pollutant type, and experiment factors play vital roles in the photodegradation process. In this regard, the effect of reaction conditions such as pH, concentration of photocatalysts, and pollutants on degradation efficiency requires further investigation. Therefore, the results obtained so far sustain the performance of zeolite-based photocatalysts in the degradation of organic pollutants and their use in practical environmental applications.

Here, Fe, Co, Ni/Ti-containing zeolite Y photocatalysts were obtained, characterized, and utilized in the degradation of cefuroxime (β-lactam antibiotic) from water. Scavenger experiments were performed to deepen the photodegradation mechanism. Titanium was immobilized, as tetrahedral coordinated Ti in the zeolite Y framework, during the sol-gel process from the zeolite synthesis. Subsequently, Fe, Co, and Ni oxides (5 %) were immobilized on the prepared Ti-containing zeolite Y support by impregnation method. X-ray diffraction, N_2 physisorption, H_2-TPR, XPS, Raman, UV-Vis and photoluminescence spectroscopy were used to investigate the structure, texture, composition, configuration, and optoelectronics properties of the photocatalysts. The results obtained in this study, both for titanium and second 3d metal species (Fe, Co, Ni), were compared with those obtained for similar photocatalysts with titanium immobilized on zeolite Y by impregnation [19, 30].

2. Results and Discussion

2.1. Structura, morphological and textural properties

2.1.1. X-Ray Diffraction

Structural analysis of zeolites was performed using X-Ray diffraction (XRD) and transmission electron microscopy (TEM). XRD patterns of the samples with Fe, Co, and Ni supported on Ti-zeolite Y are presented in Figure 1. The results mainly indicate the characteristic peaks of faujasite Y. It means that the addition of 3d metal oxides, but especially the incorporation of titanium into the aluminosilicate gel framework did not affect the obtaining of the crystalline structure of zeolite Y. It was proven in studies previously reported by our group [19, 20] that the proposed synthesis method succeeds in obtaining titanium-aluminosilicate with the Y faujasite structure for TiO_2 concentrations lower than 5 %. The presence of titania in the synthesized materials was confirmed by X-ray fluorescence, the results obtained being 1.1 % for a theoretical concentration of 1 % and 2.3 % for a theoretical concentration of 2 %.

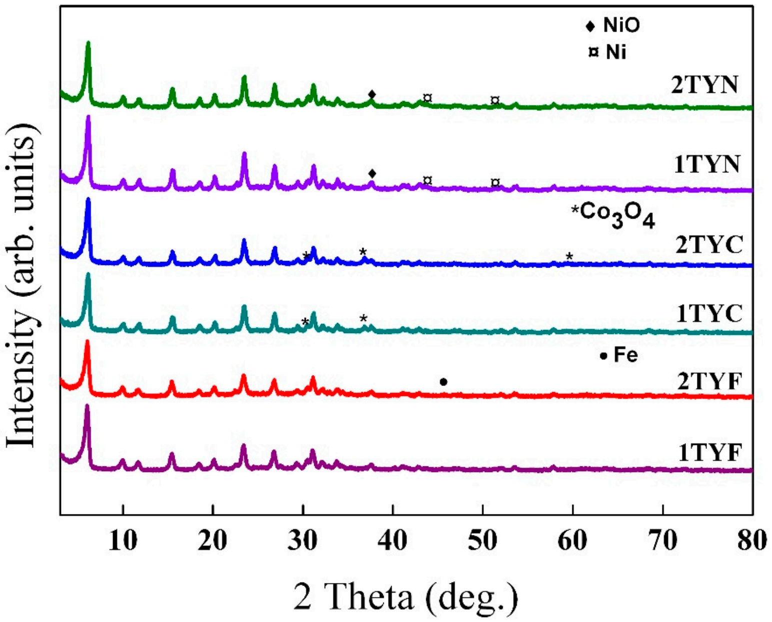

Figure 1. XRD patterns of the samples.

In the case of samples modified with cobalt oxide, the XRD results show the formation of Co_3O_4 crystalline phase. Thus, the peaks located at 31.19°, 36.84°, and 59.31° were attributed to the Co_3O_4 crystal faces (220), (311), and (511), respectively. Modification of Ti-zeolite Y supports with nickel oxide led to the appearance of several discrete peaks in the XRD patterns at 37.52°, 46.76°, 63.85°, and 76.12° assigned to (111), (200), (220), and (311) planes of bunsenite NiO. Besides these, the XRD results also indicate the formation of metallic nickel. It is sustained by the presence of the peaks that appear at 43.55° and 51.42° and correspond to (111) and (200) planes of nickel in metallic form. Meanwhile, for the samples modified with iron oxide, the XRD results did not show the presence of any diffraction peak characteristic of crystalline iron oxide forms, although an experimental concentration of 3.04% was determined by XRF measurements. It is result of small iron oxide crystallites with a high dispersion, which does not allow their detection by X-ray diffraction. However, a slight signal seems to be obtained at 45.58°, suggesting the formation of metallic iron. The corresponding X-ray diffractograms of the unmodified Ti-zeolite Y supports (Figure S1) were used as a reference.

2.1.2. TEM investigation

TEM images show (Figure 2) that metal oxides are deposited on the zeolite crystals forming islands of nanometric dimensions (10-50 nm).

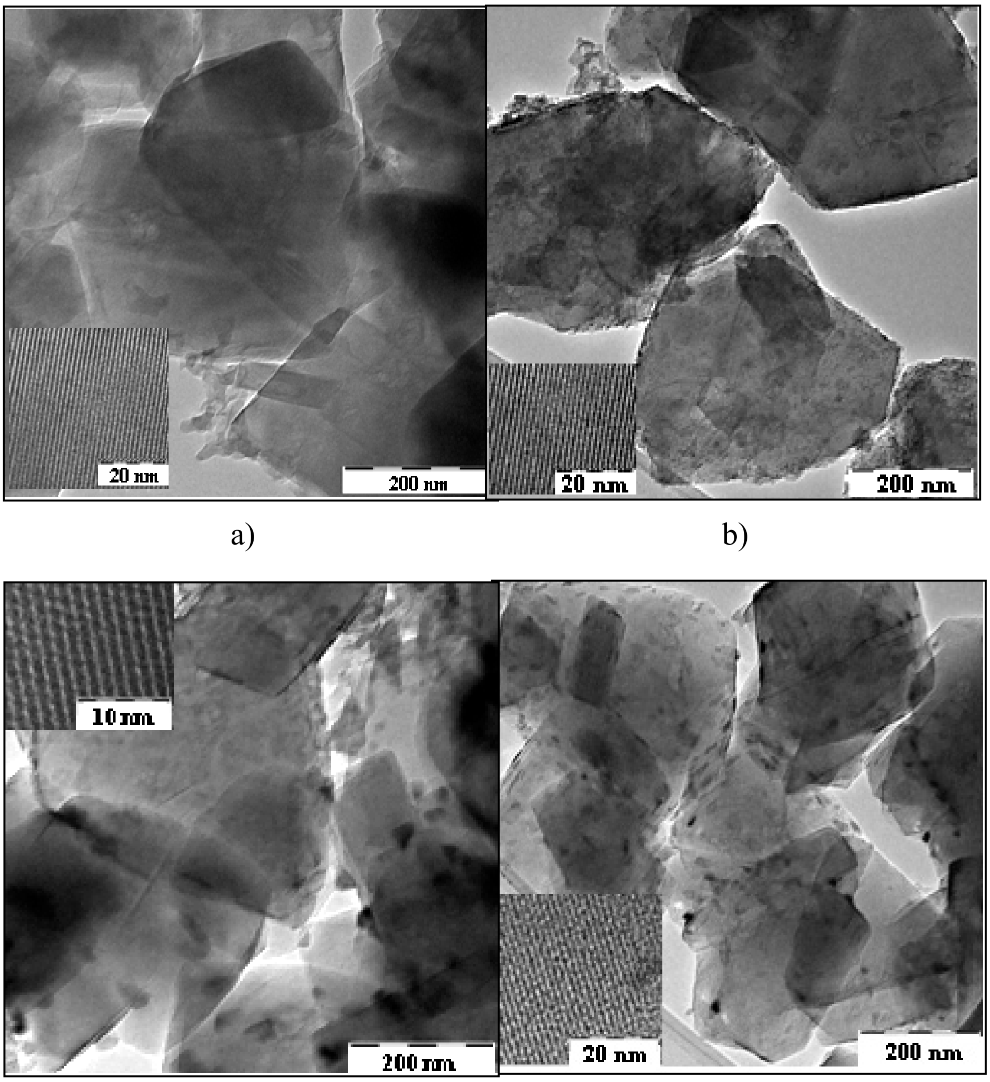

a) b)

c) d)

Figure 2. TEM images of a) 1TY, b) 1TYF, c) 1TYC, and d) 1TYN samples.

In the case of samples with Fe and Co, larger oxide phases can be observed at the interface of the zeolite crystals, which can favor their agglomeration. In the inserted TEM images can be seen the regular arrays of the zeolite Y pores of around 1 nm. After metal oxides' immobilization, irregularly stretched lines indicating crystal imperfections of Ti-zeolite Y are not observed.

2.1.3. SEM analysis

The morphology of synthesized materials was evidenced by scanning electron microscopy (SEM). SEM images of Ti-zeolite Y, before and after immobilization of Fe, Co, Ni oxides, are presented in Figure 3. The typical morphology of zeolite Y (FAU zeolite), with octahedral crystals and multiple twinning polyhedrals [20, 31] are evident in all the SEM images (Figures 3a-d). A slight change in morphology, possibly due to the crystals' agglomeration, seems more visible for samples with supported iron and cobalt oxides (Figure S2). This confirms the effect of the oxide formations at the interface of the zeolite crystals highlighted in the TEM images (Figure 2b, c).

doi:10.20944/preprints202312.0455.v1

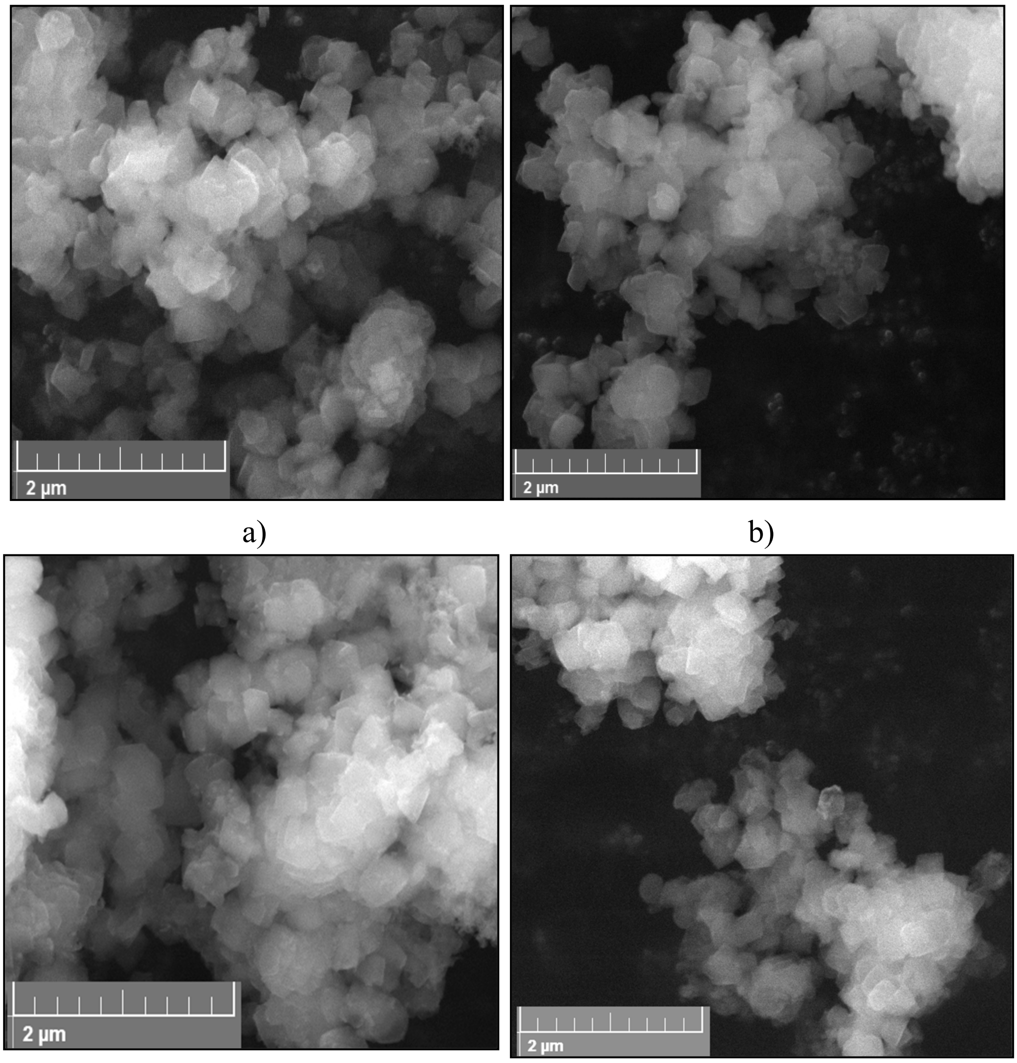

a) b)

c) d)

Figure 3. SEM images of a) 1TY, b) 1TYF, c) 1TYC, and d) 1TYN samples.

2.1.4. N_2 physisorption

Figure 4 displays the N_2 adsorption–desorption isotherms for all samples. Based on the IUPAC classification [32], all the isotherms are composites of type I(a) and type IV(a). This type of isotherm is characteristic of materials with dual-porosity generated by micro and mesopores. The isotherms exhibit hysteresis loops at relative pressures higher than 0.45 and can be classified as type H4. The textural parameters of the samples are shown in Table 1.

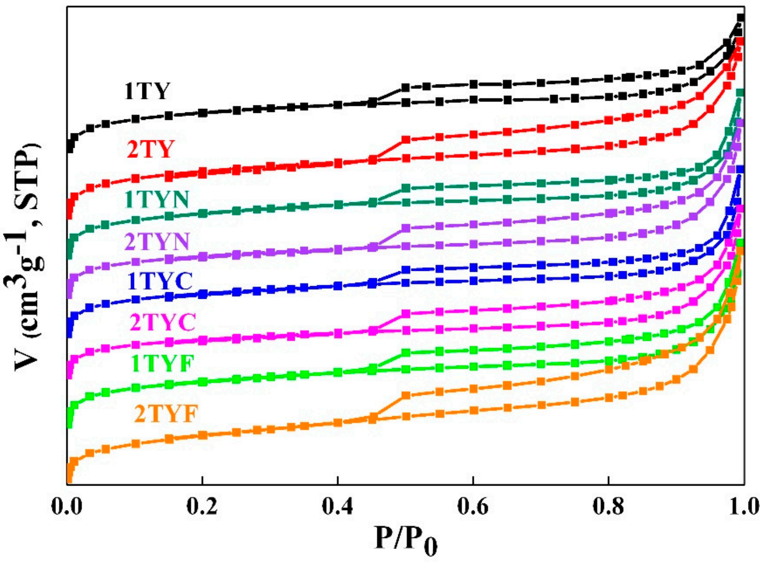

Figure 4. N_2 adsorption–desorption isotherms of the investigated materials.

Table 1. Textural parameters of the investigated materials.

Sample	BET surface area (m^2/g)	Micropore area (m^2/g)	Mesopore area (m^2/g)	Total pore volume (cm^3/g)	Micropore volume (cm^3/g)
1TY	649	585	64	0.316	0.221
2TY	591	521	70	0.320	0197
1TYC	588	532	56	0.314	0.201
2TYC	481	433	48	0.278	0.163
1TYF	573	510	63	0.319	0.193
2TYF	489	409	80	0.322	0.156
1TYN	551	484	67	0.298	0.183
2TYN	517	461	56	0.293	0.174

As can be seen, the surface area of the samples impregnated with metal oxides decreased by 10 to 20% compared to the Ti-zeolite Y supports, but the percentage of micropores and mesopores remains almost constant, 88 - 90% (micropores) and 10 – 12% (mesopores). This indicates a uniform distribution of metal oxides on the internal surface of the pores. The exception is sample 2TYF, in which the percentage of micropores is 84%, and that of mesopores is 16%. Regarding the total volume of the pores, its decrease in the samples impregnated with metal oxides compared to the support samples 1TY and 2TY is lower than in the case of the surface. It can also be seen that the decrease in total pore volume is between 1 and 13%, while the micropore volume decreases by a higher percentage, between 10 and 21%.

2.1.5. Raman spectroscopy

The UV Raman spectroscopy has been recently used for structural investigation of the surface of catalysts due to the limited penetration depth of the UV lasers [33]. Less intense and wider UV-Raman bands are present in the (1/2)TY(F/N/C) spectra in Figure 5 in contrast with the zeolite Y spectrum (372 cm^{-1}, six-membered SiO_4 rings, ~500 cm^{-1}, 4-membered SiO_4 rings, 1006 cm^{-1} and 1081 cm^{-1}, asymmetric stretching mode of the (Al/Si)-O linkages in tetrahedral coordination [34]). This is a consequence of a vitreous surface of the zeolite supported catalysts.

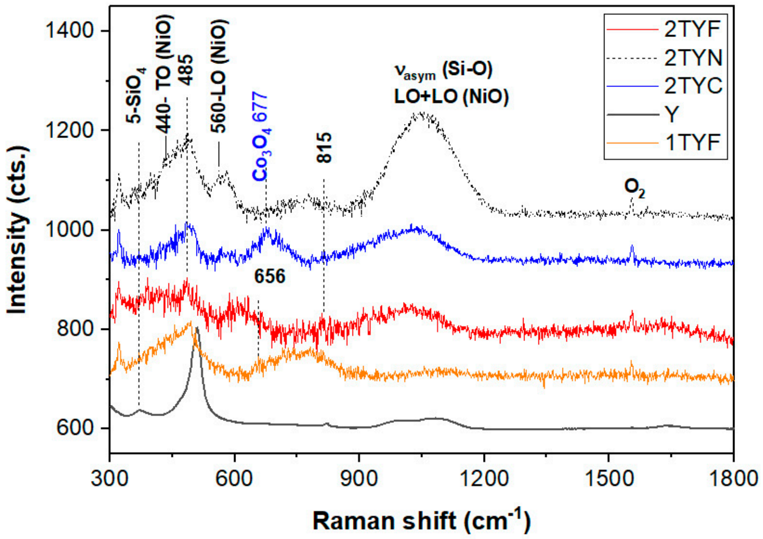

Figure 5. UV-Raman spectra of the (1/2)TY(F/N/C) samples and zeolite Y (n≤6 and T stands for Al, Ti and Si).

The tinny band at about 672 cm^{-1} belongs to the A_{1g} modes of the Co_3O_4 [35] in the 2TYC spectrum. Moreover, the spinel structure, $Co^{2+}(Co^{3+})_2O_2^{4-}$, of Co_3O_4 was identified for the (1/2)TYC samples by Vis-Raman spectroscopy (Figure S3) at 194, 485, 521, 622 and 692 cm^{-1} (F_{2g}, E_g, F_{2g}, F_{2g} and A_{1g}). A two-phonon wide band at about 1060 cm^{-1} was reported for CoO [35]. However, the later band at 1050 cm^{-1} in Figure S3 can also belong to the T-O stretch as pointed out in Table 2. Most of the NiO vibrations [36] (see Table 2) overlap those of SiO_2 [37].

Table 2. Peak position, assignments and references of the 2TY(N/C/F) and Y zeolite.

Y	2TYN	2TYC	2TYF	Assignment	Reference
372	396		391	Bending mode of double 6-membered SiO_2 rings and E_g of Fe_2O_3 (412 cm^{-1})	[34, 40]
	440	455		TO modes NiO, E_g of Co_3O_4 (470 cm^{-1}) and n-membered SiO_4 rings (n≤6)	[35, 37]
506	485	495	485	Breathing of the 4-membered SiO_2 rings (4R, 508 cm^{-1}) in 6-membered double rings (D6R, 490 cm^{-1}) and Co_3O_4	[35, 37]
	560			LO modes of NiO	[36]
	577			Al-O-Si stretching in connection with ring structures	[40]
			611	E_g modes of Fe_2O_3	[41]
			652	Symmetric Fe-O breathing A_{1g} modes	[39]
		677		A_{1g} of CoO_6 (675 cm^{-1})	[35]
		705			
	740			2TO modes of NiO	[36]
	776			O-O stretching of adsorbed O_2^{2-}	[35]
1006				Asymmetric T-O stretch (T=Al and Si)	[34]
	1054	1032	1027	Asymmetric T-O stretch (T=Al, Ti and Fe) and two-phonon modes of CoO	[35, 37]
1081				Asymmetric T-O stretch (T=Al and Si)	[34]

Given the low titania content and lack of the Raman bands of the anatase (398 cm^{-1}, B_{1g}, and 633 cm^{-1}, E_g) and/or rutile (611 cm^{-1} and 826 cm^{-1} due to A_{1g} and B_{2g} modes [38]) in Figure 5, tetrahedral framework titanium atoms were obtained in the (½)TY(F/N/C) powders by adding titanium acetylacetonate to the alumiosilicate gel, according to the synthesis method.

Given the strong UV adsorption due to the ligand-to-metal charge transfer transition of O^{2-}—Fe^{3+}→O^{-}—Fe^{2+} was reported to occur below 300 nm [39], the Fe-O-Si bonds in a zeolite framework give only faint Raman signals regardless of the iron oxide content when an exciting laser line of 325 nm is used. Fan et al. [40] reported that Raman bands (collected with 244 nm laser closed to the charge transfer transition) at about 516 and 1115 cm^{-1} in the Fe-ZSM-5 belong to the symmetric and asymmetric stretching modes of the Fe-O-Si bonds of the tetrahedral coordinated Fe^{3+}. In the case of the 2TYF sample, the 1115 band might be obscured by the stronger Si-O stretching modes peaking up at 1027 cm^{-1} or extra-framework iron species (magnetite and/or hematite) are present. The latter species should be confirmed by UV adsorption bands or shoulders at about 350 nm and 480 nm for hematite [39] (see below 2.3).

2.2. Composition and reduction of photocatalysts

2.2.1. XPS spectroscopy

The elemental composition and the chemical states of the sample surfaces were measured by X-Ray Photoelectron Spectroscopy (XPS). The XPS survey (Figure 6) shows the following core levels: O 1s, Si 2p, Al 2p, Na 1s, C 1s, Ti 2p, Co 2p, Ni 2p and Fe 2p. The analyzed fitted spectra of Fe 2p, Co 2p and Ni 2p (Figures 7 and 8) revealed the coexistence of different chemical states of each metal.

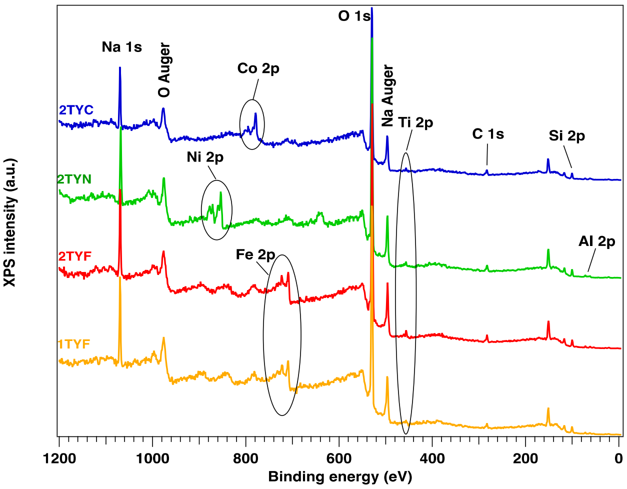

Figure 6. XPS full scan survey spectra for the samples, indicating all the elements.

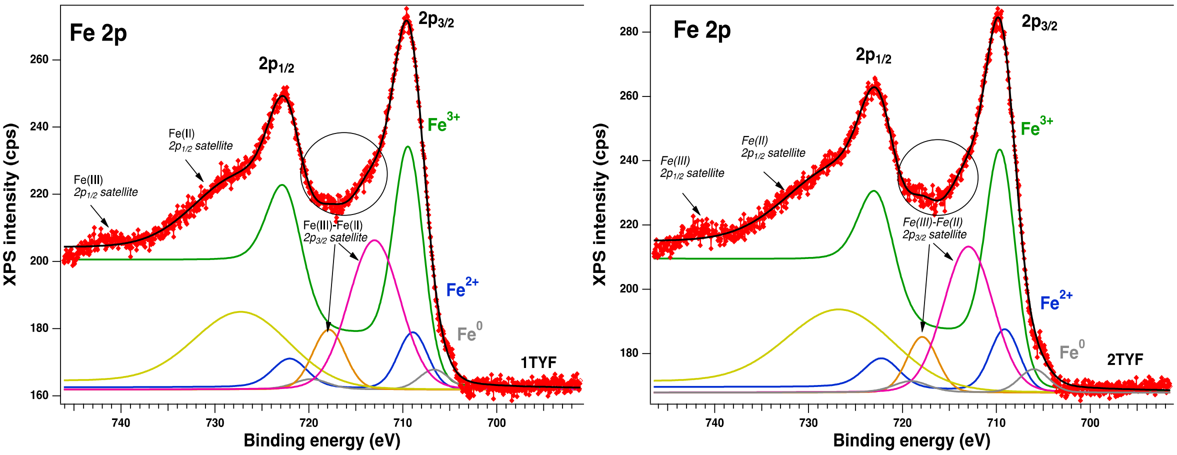

Figure 7. XPS spectra of Fe 2p (a) for the samples 1TYF and 2TYF, and their deconvolutions with the interpretation. Red symbols – raw data, black line – fit, grey, blue and green lines – the main components; the other components are the satellites of Fe(II) and Fe(III).

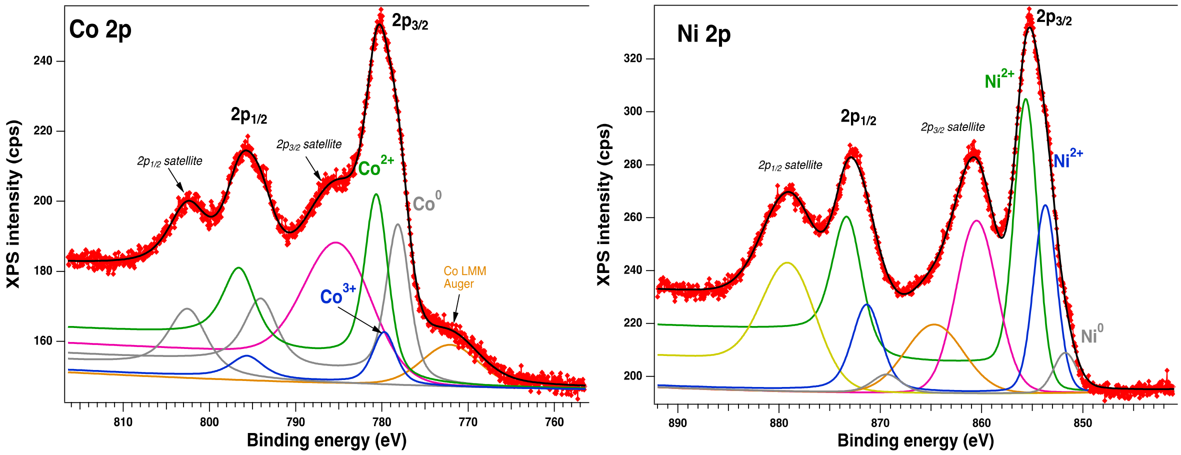

Figure 8. Fitted XPS spectra of Co 2p (Red symbols – raw data, black line – fit, blue and green lines – the main components; the other components are the satellites and the Auger line of Co 2p) and of Ni 2p (Red symbols – raw data, black line – fit, grey, blue and green lines – the main components; the other components are the satellites of Ni 2p).

The spectra were fitted using the same algorithm as in the previous research [30]. As it was mentioned previously, all the core levels of interest were analyzed using Voigt profiles, where each component has their own background and could give supplementary information. The component with highest background suggests that its signal is coming from the "bulk", whereas the component with lowest backgound is from the top surface. The samples with Fe 2p showed up three chemical states (Figure 7), according to the database: metallic (~707 eV), Fe^{2+} (~709 eV), Fe^{3+} (~709.5 eV) [42]. Co 2p presents (Figure 8) two main components and their satellites, at binding energies (BE) of 778.2 eV and 780.5 eV, attributed to the metal and 2+ chemical states [30, 43] with a spin orbit splitting of ~15.8 eV. The Ni 2p core level is illustrated in Figure 8 and the fitting revealed the coexistence of two chemical states: Ni^0 - 851.7 eV (a small amount), Ni^{2+} - 853.7 eV (NiO) and 855.6 eV ($Ni(OH)_2$), according to the tabulated data [44]. The spectra of Ti 2p for all samples shows a main component at ~458 eV attributed to Ti^{4+} (see Figure 9). This attribution is supported also by the presence of the satellite at 471-472 eV [45]. Also, it can be seen the different intensity of Ti 2p that this could be related with the interaction with the dopants.

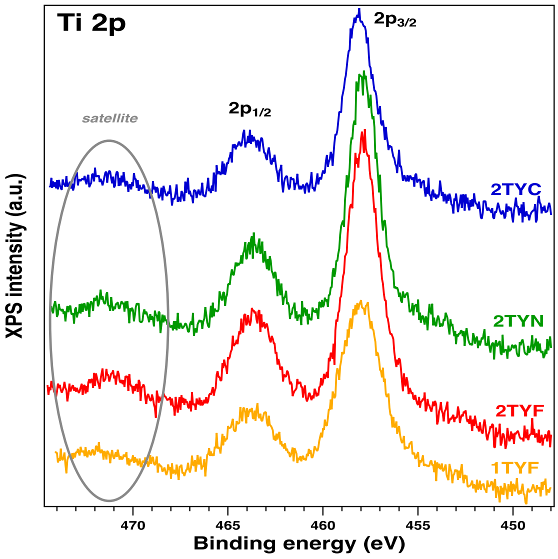

doi:10.20944/preprints202312.0455.v1

Figure 9. XPS spectra of Ti 2p for all the samples (mentioned on each spectrum).

2.2.2. H_2-Thermoprogrammed reduction

The H_2-TPR results illustrate a significant effect of metal oxides' interaction with the support. Thus, Fe, Co and Ni cations were immobilized, as oxide species, on zeolite Y support with tetrahedral Ti^{4+} isolated into the network. Under these conditions, the oxide species of these cations in mass concentration of 5% can disperse on the surface or located inside the supercages of the zeolite Y.

The location of the oxide species influences the interaction with the support and hence their reduction temperature. Also, the interaction with Ti cations, especially in the case of the isolated oxides of these transition metals from channels or cages, influences the reduction temperature. Figure 10 depicts H_2-consumption profiles for samples obtained by immobilization of Fe, Co and Ni on zeolite Y support with 2 % TiO_2. The reduction profiles obtained for Ni/Ti-zeolite Y photocatalyst (Figure 10a) present one main peak with a maximum at ~ 378 °C and a weak shoulder at around 340 °C. The shoulder is due to the reduction of free NiO species and the peak is associated with the reduction of NiO in weak interaction with the zeolite support [46, 47]. The other two peaks of lower intensity, at ~ 524 °C and 667 °C, suggest the presence of different types of NiO species in stronger interaction with the zeolite support. The XPS results (Figure 8) confirm the presence of Ni^{2+} species on the zeolite surface for this sample.

The reduction profile for 2TYF material, obtained by immobilizing iron oxide species on zeolite Y with 2 % TiO_2, shows (Figure 10a) a little shoulder at 240 °C, and two overlapping peaks with maximums at around 310 °C and 380 °C that can be connected to the conversion of Fe_2O_3 to Fe_3O_4 [48, 49]. The first peak can be attributed to the reduction of the isolated Fe^{3+} species to Fe^{2+} and the second, broader one, to the oxide which are probably located inside the supercages by different coordination with the framework oxygen atoms [50, 51]. The last broad peak at around 600 °C can be related to the conversion of Fe_3O_4 to FeO. The iron oxide species which interact more or less strongly with the zeolite support justify this broad peak of 2TYF sample reduction profile. The XPS spectra (Figure 7) of samples 1TYF and 2TYF indicate the presence of Fe^{2+}, Fe^{3+} and also Fe^0 on the surface. The fact that part of the iron species is already reduced to Fe^{2+} and their reduction to Fe^0 can take place at higher temperatures (around 800 °C) justifies the reduced volume of hydrogen consumed compared to 2TYN (Figure 10a).

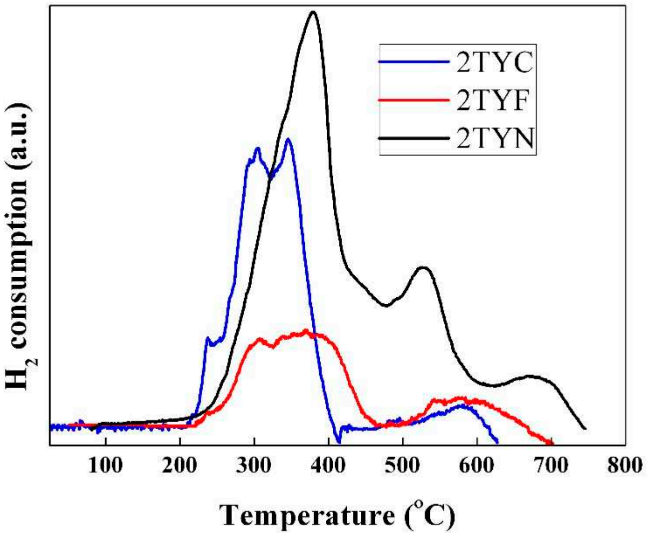

(a)

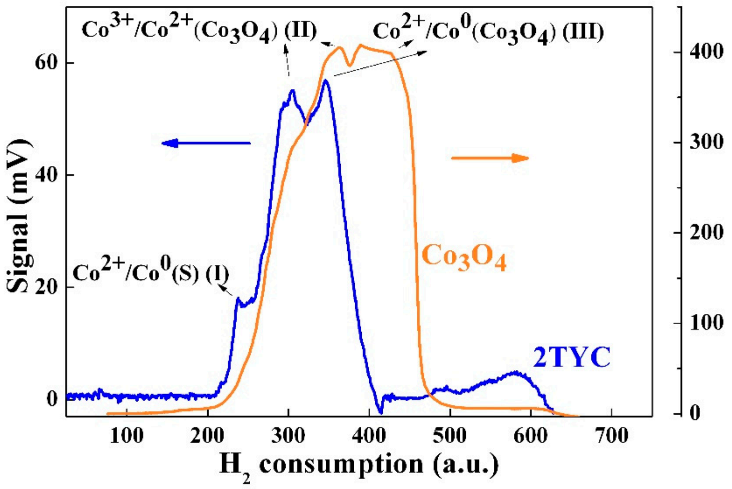

(b)

Figure 10. (a) H_2-TPR profiles of samples with Fe, Co and Ni oxides supported on zeolite support with 2% TiO_2, and (b) H_2-TPR comparative profiles of supported and commercial Co_3O_4 oxide.

For 2TYC sample containing supported cobalt oxides, were obtained reduction peaks at ~ 240°C, 300°C, 350 °C and 580 °C. Compared to the pristine (Figure 10b), two reduction peaks were detected for pure Co_3O_4, at around 360 °C attributed to the reduction of Co^{3+} to Co^{2+} and at ~ 450 °C corresponding to the reduction of Co^{2+} to Co^0 [52, 53]. These peaks are shifted, for sample 2TYC, to lower temperatures (300 °C and 350 °C). Due to the dispersion on the support, both hydrogen adsorption and its interaction with the oxide species are favored. The XPS results (Figure 8) showed the presence of Co^{2+}, Co^{3+} and Co^0 on the surface of 2TYC sample. The broader peak with a maximum at approximately 600 °C, only for supported cobalt oxide, may be due to a stronger interaction of Co^{2+} species with the support. In Figure 10 each H_2-consumption profile show a shoulder or a peak, between 200°C and 300 °C. Each shoulder is assignable to the adsorption on the surface of hydrogen. In the case of samples 2TYC and 2TYF, the peak and respectively little shoulder at ca. 240 °C from the H_2-consumption profiles can be due to the hydrogen spillover effect. For Fe_2O_3 supported on ZSM-5 zeolite, the effect of Fe^0 and other transition metals on hydrogen atoms' migration (H_2 spillover) and the reduction of oxides were observed [51]. Thus, in the case of 2TYF and 2TYC samples, the spillover effect can be favored by the Fe^0 and Co^0, evidenced by XPS spectroscopy (Figures 7 and 8), and by Ti^{4+} from the gel network of the zeolite Y support.

2.3. Optical properties

2.3.1. UV-Vis spectroscopy

The optical properties of the synthesized materials were evaluated by UV-Vis absorption spectroscopy. The recorded spectra are presented in Figure 11 and suggest the successful incorporation of Ti in the aluminosilicate gel framework of zeolite Y. It is supported by the absorption band located at 210 nm, assigned to the ligand-to-metal charge transfer $Ti^{4+}O^{2-} \rightarrow Ti^{3+}O^{-}$ [54]. An additional broad absorption band appeared toward higher wavelength (250 nm), more visible for the samples with a higher Ti content (2 %), and indicates the formation of extra-framework Ti species [54, 55]. The small shoulder located at 330 nm is usually assigned to anatase traces.

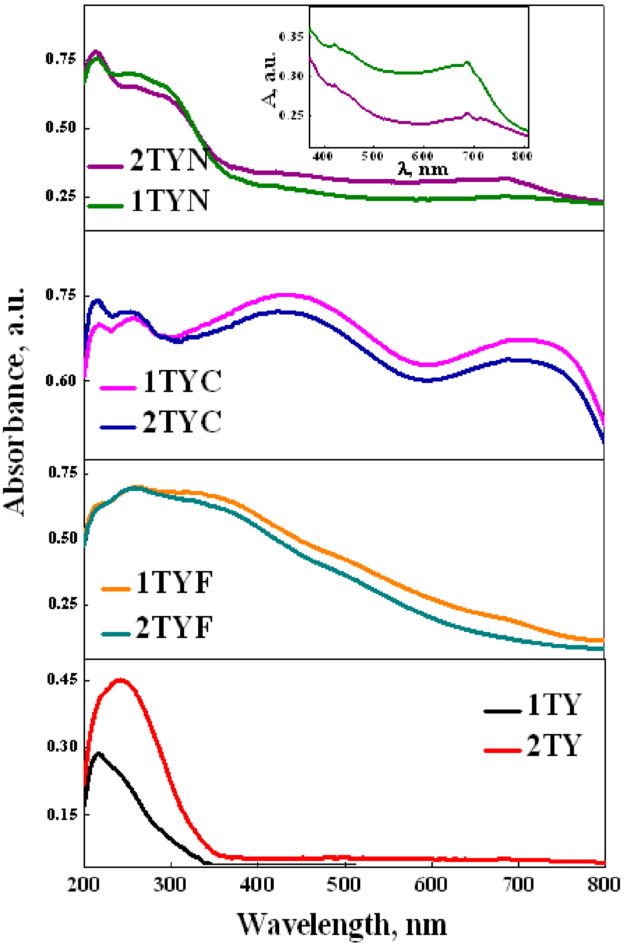

Figure 11. UV−Vis absorption spectra of the synthesized photocatalysts. .

A strong redshift of absorption spectra was observed after iron oxide immobilization, given by the charge transfer of oxygen to octahedral Fe^{3+} from Fe_2O_3 nanoparticles. In addition, the band located at 350 nm suggests the formation of some extra-framework FeOx oligomers [56]. Also, Co-modified materials present two intense absorption bands in visible range with maximums located at 440 and 710 nm, assigned to the charge transfer transition $O^{2-}\rightarrow Co^{2+}$ and $O^{2-}\rightarrow Co^{3+}$ [30, 57]. Modification of Ti-zeolite Y supports with nickel oxide led to a slight broadening of the absorption band in the UV range, due to $O_2\rightarrow Ni^{2+}$ charge transfer which overlapped with the absorption bands given by the titanium species. Also, it was observed the appearance of two new broad absorption bands in the visible range located at 420 nm and 690 nm. These are related to $^3A_{2g}\rightarrow {}^3T_{1g}$ (P) and $^3A_{2g} \rightarrow {}^3T_{1g}$ (F) transitions (Table 3) given by the presence of Ni^{2+} ions in octahedral or pseudo-octahedral symmetry [58, 59].

Table 3. Assignments of the absorption peaks recorded for the samples.

Sample	Absorption peak position	Assignment	Ref.
1TY 2TY	210 nm	framework Ti species ($Ti^{4+}O^{2-} \rightarrow Ti^{3+}O^{-}$ charge transfer)	[54]
	250 nm	extra-framework Ti species	
	330 nm	anatase traces	
1TYF	260 nm	charge transfer of oxygen to Fe^{3+} cations in octahedral coordination	
	350 nm	extra-framework FeO_x oligomers	[56]

doi:10.20944/preprints202312.0455.v1

2TYF	480 nm	oxygen-to-metal charge transfer transitions that involve octahedral Fe^{3+} species	
1TYC	440 nm	$O^{2-} \rightarrow Co^{2+}$ charge transfer transition	[30, 57]
2TYC	710 nm	$O^{2-} \rightarrow Co^{3+}$ charge transfer transition	
1TYN	420 nm	$^3A_{2g} \rightarrow {}^3T_{1g}$ (P) charge transfer transition	[60]
2TYN	690 nm	$^3A_{2g} \rightarrow {}^3T_{1g}$ (F) charge transfer transition	

The band gap energies of all the samples were obtained using the Kubelka-Munk function, by plotting $(h\nu \cdot F(R\infty))^{1/2}$ versus photon energy. The values are summarized in Table 4 and showed a decrease compared with pristine TiO_2 (3.2 ev [61]). An important narrowing of the band gap energy was observed by modifying the Ti-zeolite Y support with iron and cobalt oxide, obtaining values below 1.5 eV (Table 4). It means that less energy is required for e^- transfer, improving the photocatalytic process. Although the immobilization of nickel oxide also leads to a decrease in the energy of the band gap, the effect is not as important as in the case of iron and cobalt oxides.

Table 4. Band gap values of the photocatalysts.

Sample	1TYF	1TYN	1TYC	2TYF	2TYN	2TYC
Eg (eV)	1.23	2.74	1.30	1.42	2.92	1.26

2.3.2. Photoluminescence spectroscopy

The photoluminescence (PL) technique has been used to investigate the effect of 3d metals, from the VIII group, on the optical and photochemical properties of Ti-zeolite Y. The recorded PL spectra of Ti-zeolite Y and Fe/Co/Ni-modified Ti-zeolite Y, using an excitation wavelength of 320 nm are shown in Figure 12. Ti-zeolite Y materials with different amounts of TiO_2 display two clear PL emissions peaks related to the indirect band-to-band recombination of photo-generated electron-hole pairs (in the high energy range) [62] and to the self-trapped excitons (STE) formed by electrons binding to the oxygen vacancies and defects, respectively (in the low energy range) [60, 62, 63].

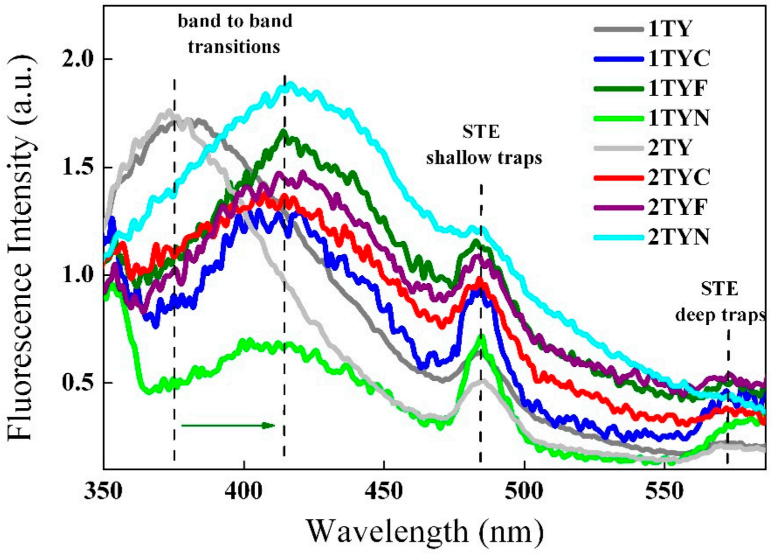

Figure 12. PL spectra of Ti-zeolite Y and Fe/Co/Ni modified Ti-zeolite Y with different TiO_2 content ($\lambda_{exc.}$=320 nm).

Modification of aluminosilicate gel containing titanium in the network with oxides of 3d metals from VIII group leads to obtaining three obvious PL signals at about 415, 485, and 575 nm, respectively. It is reported that the bands appearing in the visible range are mainly related to surface defects, band edge-free excitons, and oxygen vacancies [64-66]. The type of dopant species like Fe, Co, or Ni seems to have an important effect on the photoluminescence properties due to the different effects on the separation of photo-generated electron(e^-)/holes(h^+) pairs and their recombination process. Figure 12 shows that the post-synthesis modification of aluminosilicate gel containing titanium in the network with cations of 3d metals, from the VIII group, led to a shift in the lower energy range and to a quenching of the first PL emission signal. This is most probably due to the formation of some sub-bands (surface states) by the addition of 3d metallic species, so the transfer of excited electrons from the bottom of the conduction band to the top of the valence band takes place via new sub-bands through a non-radiative process firstly and a radiative one, secondly [67]. The formation of new sub-bands leads to a delay in the electron-hole repairing, which is desirable in photocatalysis. The second PL signal seems to keep its position, but increases in intensity after the immobilization of 3d metallic oxides. It is related to the formation of new oxygen vacancies and defects as shallow trap centers, iron oxide having the most pronounced effect, followed by cobalt oxide. Also, the results showed a new broad PL band appearing in the lower energy domain, assigned to the deep defects and oxygen vacancies [60, 63].

2.4. Photocatalytic activity

2.4.1. Photocatalytic degradation of cefuroxime

The photocatalytic performances of the samples were evaluated in the degradation of cefuroxime (β-lactam) antibiotic from water under visible light irradiation. The results are shown in Figure 13 and indicate the highest degradation efficiencies for the samples modified with iron oxide. This is explained by the lower value of the band gap energy (1.23 eV for 1TYF and 1.30 eV for 2TYF, Table 4), thus contributing to the electron transfer process under visible light irradiation.

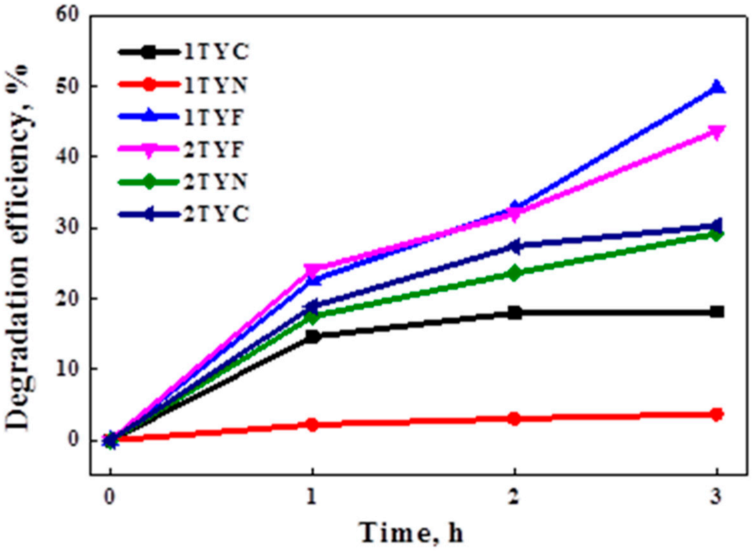

Figure 13. Photocatalytic performances of the samples under visible light irradiation.

Noteworthy, the photocatalytic activity of Ti - aluminosilicate gel modified with transition metals from VIII group (Fe, Co, Ni) exhibits a direct relationship with the PL signals associated with surface trape excitons processes. It suggests the important effect of oxygen vacancies and defects obtained during the synthesis, which binds the photogenerated electrons preventing e^-/h^+ pairing and thus improve their availability to further interact with oxygen molecules adsorbed on the surface and generate superoxide radicals, active in the degradation process.

It was shown that in the process of TS-1 doping with Fe or Ni, the migration of electrons is from iron species to the support, respectively from the support to nikel species [68]. The different interaction with the support and different energies of valence and conduction bands of the photocatalysts with Fe and Ni compared to Ti-containing zeolite support influence the mechanism of the photocatalytic reaction, as well as the degradation efficiency (Figure 13). The proposed mechanisms of cefuroxime degradation over the prepared photocatalysts are presented in Figure 14.

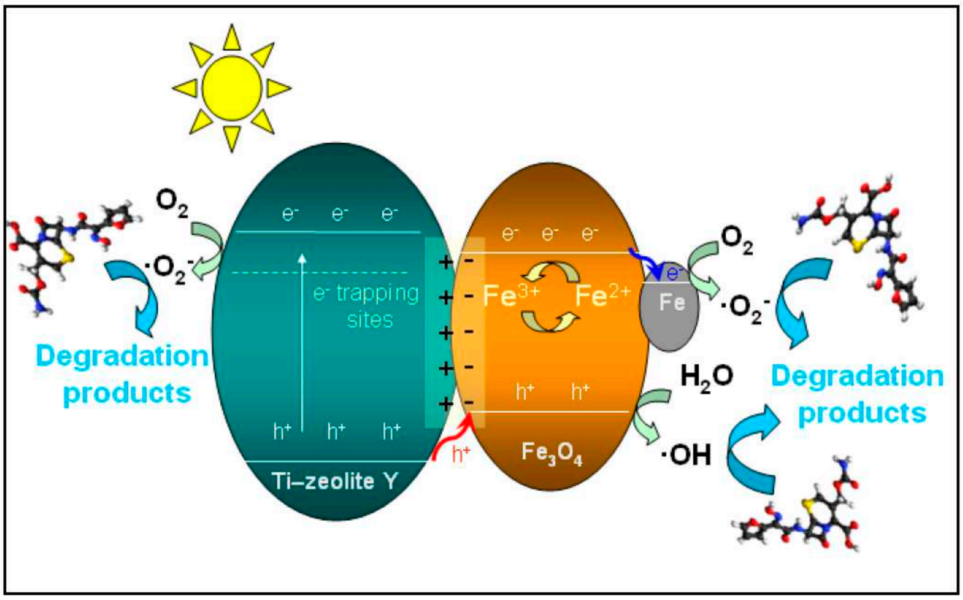

(a)

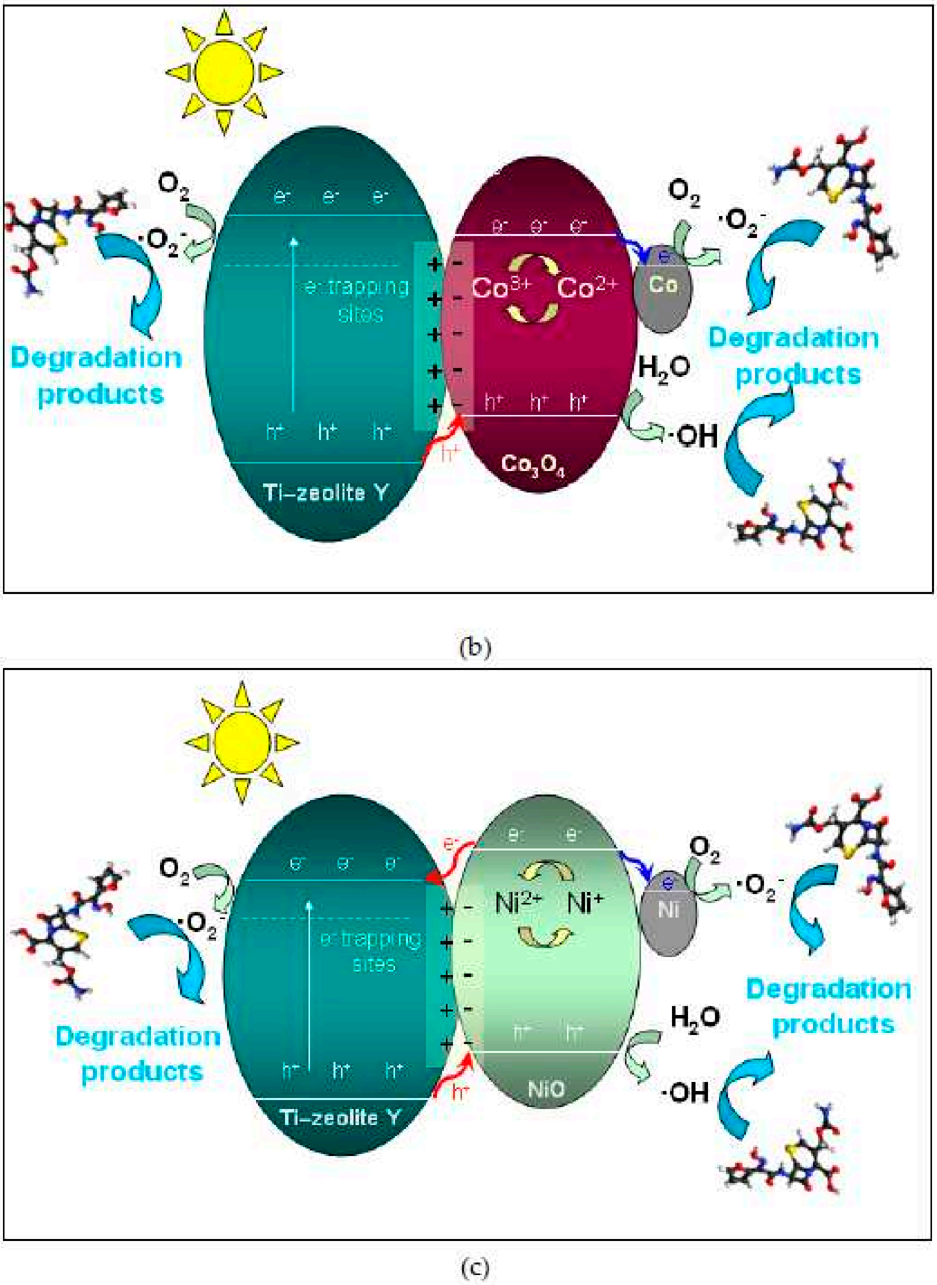

Figure 14. Possible mechanism of photocatalytic degradation of cefuroxime over Ti-zeolite Y modified with Fe, Co or Ni oxides.

Adding various p-type semiconductors such as Fe_3O_4, Co_3O_4 and NiO on Ti-containing zeolite Y (n-type semiconductor) with titanium incorporated in the network leads to the formation of a p-n type heterojunction. There is an internal electric field that ensures the spatial separation of the photogenerated charge carriers and directs the transfer of holes from an n-type semiconductor to a p-type semiconductor and the transfer of electrons in reverse [68]. According to the band edge position, a difference appears between the three types of synthesized materials. As can be seen in Figure 14, while the holes generated in the valence band (VB) of TiO_2 are transferred to the VB of all the used p-type semiconductors, the electrons transfer from the conduction band (CB) of p-type semiconductors to the CB of TiO_2 is allowed only for NiO. However, there is a transfer of electrons from the conduction band of the 3d metal oxides (Fe_3O_4, Co_3O_4, NiO) to the metallic species formed, as was suggested by the XPS data (Figures 7 and 8), for each of the three types of photocatalytic systems. Thus, the recombination of e^-/h^+ pairs is reduced.

Meanwhile, the high dispersion of iron oxide, as was suggested by XRD results, ensures an efficient p-n heterojunction and hence a better separation of photogenerated charge, improving the photocatalytic performances. Under light irradiation, the separated electrons and holes are available to interact with O_2 and H_2O from the reaction medium, leading to generation of different reactive species, free to degrade the cefuroxime molecules. As illustrated in Figure 14, the photogenerated electrons reduce O_2 producing superoxide ($\cdot O_2^-$) radicals, while the separated holes oxidize H_2O molecules, forming hydroxyl (·OH) radicals in the system. These two reactive oxygen species thus obtained are considered to be the main ones involved in the photocatalytic degradation of organic pollutants in water [70-72]. To further investigate the degradation mechanism and to clarify the role of each reactive species, scavenger experiments were carried out.

2.4.2. Scavenger experiments

Exploration of the degradation mechanism depending on the type of 3d metal oxide supported on Ti-incorporated zeolite Y was performed using different quenching molecules which interact specifically with the main reactive species resulting under irradiation.

As shown in Figure 15, the scavenger addition in the reaction system led to a distinct decrease in the efficiency of cefuroxime degradation, indicating that several reactive species are involved in the process. The addition of the h^+ scavenger had a moderate decreasing effect on the photocatalytic efficiency, indicating that the photogenerated holes also participated in the degradation process. For all the samples was observed that the addition of p-BQ significantly decreased the degradation reaction, suggesting that $\cdot O_2^-$ radicals played a key role in the oxidation of cefuroxime.

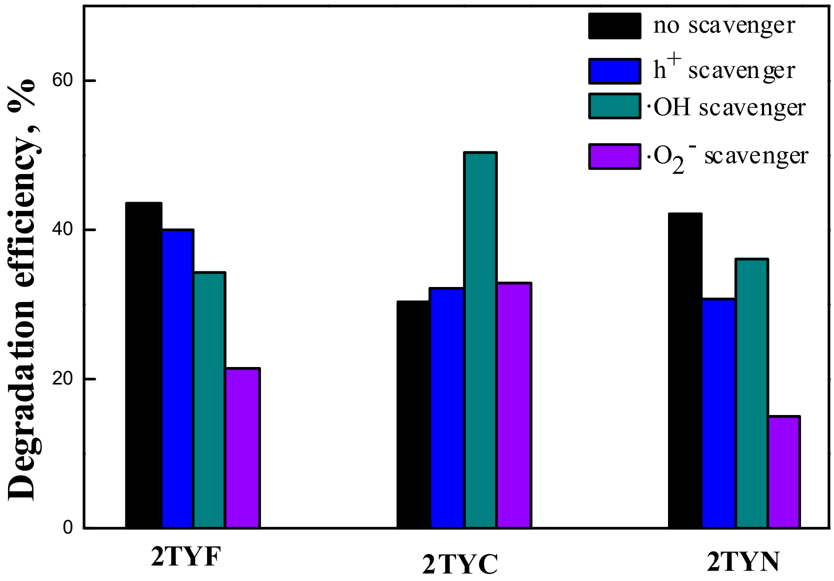

Figure 15. Scavenger experiments for the photocatalytic degradation of cefuroxime using Ti-zeolite Y modified with Fe, Co, or Ni oxides.

A considerable decrease in the photocatalytic efficiency by adding $\cdot O_2^-$ scavenger was found in the case of the sample modified with Ni oxide, suggesting that for this material, the degradation of cefuroxime takes place mainly through superoxide species. This behavior can be explained by the higher probability of the superoxide radical formation, led by a better separation of electrons-holes pairs. The significant increase of efficiency for 2TYC photocatalyst in the presence of the ·OH scavenger evidenced the effect of 3d metal oxides and their interaction with Ti-incorporated into the zeolite Y gel network on quenching molecule degradation.

3. Conclusions

doi:10.20944/preprints202312.0455.v1

In the present work, an aluminosilicate gel was used as a raw material for the synthesis of efficient photocatalysts for the degradation of β-lactam antibiotics. Titanium was incorporated in different concentrations (1 and 2%) into the zeolite network by modifying the gel during the zeolitation process. A serie of 3d metals from VIII group, such as Fe, Co, and Ni was supported on Ti-containing zeolite Y and their photocatalytic properties were studied. H_2-TPR, Raman, XPS and UV-Vis spectroscopy results showed the formation of Fe_3O_4, Co_3O_4, and NiO along with small amounts of metals for all obtained samples. These species and their interaction with support facilitated the charge separation across the p-n heterojunction interface and also the presence of oxygen vacancies and surface defects which can bind the photogenerated electrons. The influence of metallic species that receive electrons from the conduction band of the corresponding oxide on the photocatalytic reaction mechanism and the effect of each metal oxide on degradation efficiency was also evidenced. The best results were obtained for iron-supported samples.

4. Materials and Methods

4.1. Materials

4.1.1. Chemicals

For the synthesis of titanium-zeolite Y supports were used sodium silicate solution (26.5 wt. % SiO_2, 10.6 wt. % Na_2O), sodium aluminate ($NaAlO_2$), and titanium acetylacetonate ($((CH_3)_2CHO]_2Ti(C_5H_7O_2)$). The basic medium required for the zeolitization process was ensured by using NaOH (98 wt%). All the chemicals were purchased from Sigma-Aldrich. The post-synthesis modification of the supports were made by using iron (III) nitrate nonahydrate ($Fe(NO_3)_3{\cdot}9H_2O$ (Sigma Aldrich), nickel (II) nitrate ($(Ni(NO_3)_2{\cdot}6H_2O)$, and cobalt (II) nitrate ($(Co(NO_3)_2{\cdot}6H_2O)$ from Merck (Darmstadt, Germany).

For the photocatalytic experiments was used cefuroxime ($C_{16}H_{16}N_4O_8S$) and for scavenger experiments, potassium iodide (KI), ethanol (C_2H_5OH) and p-benzoquinone ($C_6H_4O_2$). All of these chemicals were purchased from Merck (Darmstadt, Germany).

4.1.2. Sample Preparation

Titanium containing Y zeolite materials with different titanium concentrations (noted xTY, x = 1, 2) were obtained by a seed-assisted method. This method ensures the incorporation of titanium into the aluminosilicate gel network corresponding to zeolite Y by direct synthesis, using titanium acetylacetonate as a titanium precursor. The two sol-gels prepared as has been described before by our group [20] were hydrothermally treated to obtain the crystalline structure specific to faujasite Y. After filtration, the precipitates were washed with deionized water, dried at 60 °C, and calcined at 600 °C.

The two supports thus obtained were further modified with 5 wt. % 3d metal oxide by impregnation method, using aqueous solution of $Fe(NO_3)_3$, $Co(NO_3)_2$ or $Ni(NO_3)_2$. The samples were firstly dried at room temperature overnight and then at 100 °C for 8 hours. Co and Ni-modified photocatalysts were calcined at 450 °C for 6 hours and Fe-modified samples at 500 °C for 5 hours in air with a heating rate of 2 °C/min. The obtained materials were noted as xTYMe, where x is 1 or 2 and represents the concentration of titanium species, and Me is the 3d metal used for impregnation (Fe, Co, or Ni).

4.2. Methods of Characterization

X–ray diffraction (XRD) patterns were recorded using a Rigaku Ultima IV diffractometer (Rigaku Corp., Tokyo, Japan) with Cu Kα (λ = 0.15406 nm).

Elemental analysis of the samples was performed in vacuum using a Rigaku ZSX Primus II spectrometer (Tokyo, Japan). The results were analyzed using EZ-scan combined with Rigaku SQX fundamental parameters' software (standard less) which is capable of automatically correcting all matrix effects, including line overlaps. Structure and morphology were evidenced by transition

doi:10.20944/preprints202312.0455.v1

electron microscopy using a JEOL 2100 TEM microscope (Tokyo, Japan) and scanning electron microscopy by TESCAN Lyra3 XMU SEM microscope (Brno, Czech Republic).

The textural characterization of the samples was performed by N_2 physisorption analysis using a Micromeritics ASAP 2020 instrument (Norcross, GA, USA). The samples were degassed under vacuum for five hours at 300 ^{0}C before each measurement. The BET model was used to calculate the apparent surface areas from the adsorption branches, while the amount of nitrogen adsorbed at the relative pressure of 0.99 was used to calculate the total pore volume. The micropore and mesopore volumes, together with the micropore and mesopore surface areas were calculated using the t-plot method.

The XPS spectra were obtained using an AXIS Ultra DLD (Kratos Surface Analysis, Manchester, UK) setup, using Al Kα1 (1486.74 eV) radiation produced by a monochromatized X-Ray source at operating power of 144 W (12 kV × 12 mA). The survey spectra were recorded using hybrid lens mode, 160 eV pass energy, slot aperture and the high resolution spectra were measured with a 40 eV pass energy. The binding energies scale was calibrated to the standard value of C 1s, 284.6 eV. The core level spectra were analyzed using Voigt profiles, based on the methods described in ref. [73].

Hydrogen temperature-programmed reduction (H_2-TPR) of the samples was performed by means of a ChemBET 3000-Quantachrome (USA) with a thermal conductivity detector (TCD). A continuous flow of 5 vol% H_2 in Ar (70 mL/min) over 50 mg of photocatalyst was used and a heating rate of 10 °C /min.

The UV -Raman spectra of the xTY(F/N/C) samples were recorded using a LabRam HR800 spectrometer (Horiba France SAS, Palaiseau, France) equipped with a 325 nm laser line. Vis-Raman spectra of the (½)TYC samples were collected by means of a Jobin-Yvon T64000 spectrometer (Horiba Jobin-Yvon, Palaiseau, France). The samples were analyzed with a wavelength of 532 nm and a power of 0.5 mW.

DR-UV/Vis spectroscopy was used to detect the coordination states of 3d metallic species added to zeolite Y framework during the synthesis (in the case of Ti) or post-synthesis by impregnation method (for Fe, Co, Ni). The spectra of the samples were recorded by means of a JASCO V570 spectrophotometer (Tokyo, Japan) in the range of 200–1000 nm.

The photoluminescence spectra of the powders were recorded by means of an FLSP 920 spectrofluorimeter (Edinburgh Instruments, Livingston, UK) with a Xe lamp as an excitation source (λ_{exc}=320 nm). For all measurements, excitation and emission slits were 7 nm.

The photocatalytic tests were conducted under stirring in a closed room at 30 °C by adding 10 mL aqueous solution of cefuroxime, CFX (5 mg/L) and 20 mg of the photocatalyst. The reaction mixture was stirred in darkness for 30 minutes to allow the adsorption of cefuroxime molecules on the hydrophobic surface of zeolite materials. Further, a halogen lamp (2x60 W) with a filter for visible light was used for irradiation. At intervals of one hour, a fixed volume of the mixture was taken out and the photocatalyst was separated using a Millipore syringe filter of 0.45 µm. The filtered solution was spectrophotometrically measured using the same JASCO V570 UV-Vis spectrophotometer, reading the maximum absorbance of CFX at λ = 280 nm. The photocatalytic degradation efficiency was obtained using the relation $(A_0\text{-}A_t)/A_0\times100$, where A is the absorbance of the solution at time t =1, 2, or 3 hours and A_0 is the initial absorbance of cefuroxime, at t=0. For scavenger experiments, 0.1 mmol of potassium iodide, ethanol and p-benzoquinone were added to the CFX solution as h^+, $\cdot OH$, and $\cdot O_2^-$ scavengers, respectively. The procedure was similar to the photocatalytic experiments. The results were presented for the case of irradiation for 3 hours.

Author Contributions: Conceptualization, V.P. and G.P.; methodology, V.P. and G.P.; validation, V.P.; formal analysis, G.P.; investigation, G.P., E.M.A., I.A., D.C.C., N.G.A., A.K., F.P., A.B. and J.L.B.; data curation, G.P., E.M.A., I.A., D.C.C., N.G.A., A.K., F.P., A.B. and J.L.B.; writing—original draft preparation, G.P., E.M.A., D.C.C., N.G.A. and V.P.; writing—review and editing, G.P. and V.P.; visualization, V.P. and G.P.; supervision, V.P. All authors have read and agreed to the published version of the manuscript.

Funding: This research received no external funding.

Institutional Review Board Statement: Not applicable.

Informed Consent Statement: Not applicable.

Data Availability Statement: The data presented in this study are available on request from the **c**orresponding author.

Conflicts of Interest: The authors declare no conflict of interest.

References

1. Hu, G.; Yang, J.; Duan, X.; Farnood, R.; Yang, C.; Yang, J.; Liu, W.; Liu, Q. Recent developments and challenges in zeolite-based composite photocatalysts for environmental applications. *Chem. Eng .J.* **2021**, 417, 129209.
2. Umejuru, E.Ch.; Mashifana, T.; Kandjou, V.; Amani-Beni, M.; Sadeghifar, H.; Fayazi, M.; Karimi-Maleh, H.; Thandiwe Sithole, N. Application of zeolite based nanocomposites for wastewater remediation: Evaluating newer and environmentally benign approaches. *Environ. Res.* **2023**, 231, 116073.
3. Camposeco, R.; Castillo, S.; Hinojosa-Reyes, M.; Mejía-Centeno, I.; Zanella, R. Effect of incorporating vanadium oxide to TiO_2, Zeolite-ZM5, SBA and P25 supports on the photocatalytic activity under visible light. *J. Photochem. Photobiol., A* **2018**, 367, 178–187.
4. Kamegawa, T.; Kido, R.; Yamahana, D.; Yamashita, H.; Design of TiO_2-zeolite composites with enhanced photocatalytic performances under irradiation of UV and visible light. *Microporous and Mesoporous Mater.* **2013**, 165, 142–147.
5. Badvi, K.; Javanbakht, V.; Enhanced photocatalytic degradation of dye contaminants with TiO_2 immobilized on ZSM-5 zeolite modified with nickel nanoparticles. *J. Clean. Prod.* **2021**, 280, 124518.
6. Farhadi, N.; Tabatabaie, T.; Ramavandi, B.; Amiri, F. Ibuprofen elimination from water and wastewater using sonication/ ultraviolet/hydrogen peroxide/zeolite-titanate photocatalyst system. *Environ. Res.* **2021**, 198, 111260.
7. Setthaya, N.; Chindaprasirt, P.; Yin, S.; Pimraksa K.; TiO_2-zeolite photocatalysts made of metakaolin and rice husk ash for removal of methylene blue dye. *Powder Technol.* **2017**, 313, 417–426.
8. Petcu, G.; Anghel, E.M.; Buixaderas, E.; Atkinson, I.; Somacescu, S.; Baran, A.; Culita, D.C.; Trica, B.; Bradu, C.; Ciobanu, M.; et al. Au/Ti Synergistically Modified Supports Based on SiO2 with Different Pore Geometries and Architectures. *Catalysts* **2022**, 12, 1129.
9. Petcu, G.; Papa, F.; Anghel, E.M.; Atkinson, I.; Preda, S.; Somacescu, S.; Culita, D.C.; Baran, A.; Ciobanu, E.M.; Jecu, L.M.; et al. Effects of Aluminosilicate Gel Treatment and TiO2 Loading on Photocatalytic Properties of Au–TiO_2/Zeolite Y. *Gels* **2023**, 9, 503.
10. Zhao, X.; Chen, W.; Li, G.; Feng, G.; Li, S.; Dong, X.; Song, Y.; Yu, X.; Chen, X.; Wei, W.; Sun, Y. Gas-phase CO_2 photoreduction via iron/ZSM-5 composites. *Appl. Catal. A Gen*. **2020**, 595, 117503.
11. John, K.I.; Adeleye, A.T.; Adeniyi, A.G.; Sani, L.A.; Abesa, S.; Orege, I.J.; Adenle, A.A.; Elawad, M.; Omorogie, M.O. Screening of Zeolites series: H-β/H-MOR/H-ZSM-5 as potential templates for photocatalyst heterostructure composites through photocatalytic degradation of tetracycline. *J. Mol. Struct.* **2023**,1277, 134852.
12. Du, T.; Cui, M.; Chao, Y.; Xiao, Y.; Ren, Z.; An, Y.; Meng. C. Preparation and photocatalytic properties of highly dispersed samarium vanadate nanoparticles supported on H-mordenite composites by template-free method. *J. Photochem. Photobiol, A* **2022**, 433, 114207.
13. Alvarez-Aguiñaga, E.A.; Elizalde-González, M.P., Sergio A. Sabinas-Hernández, *S.A.* Unpredicted photocatalytic activity of clinoptilolite–mordenite natural zeolite. *RSC Adv***.** **2020**, 10, 39251-39260.
14. Jansson, I.; Suarez, S.; Garcia-Garcia, F.J.; Sanchez, B. Zeolite-TiO_2 hybrid composites for pollutant degradation in gas phase. *Appl. Catal. B Environ.* **2015,** 178, 100–107.
15. Li, F.; Jiang, Y.; Yu, L.; Yang, Z.; Hou, T.; Sun, S. Surface effect of natural zeolite (clinoptilolite) on the photocatalytic activity of TiO_2. *Appl. Surf. Sci.* **2005**, 252, 1410-1416.
16. Tao, P.; Wang, X.; Zhao, Q.; Guo, H.; Liu, L.; Qi, X.; Cui, W. Framework Ti-rich titanium silicalite-1 zeolite nanoplates for enhanced photocatalytic H2 production from CH_3OH, *Appl. Catal. B Environ.* **2023**, 325, 122392.
17. Bai, R.; Song, Y.; Tian, G.; Wang, F.; Corma, A.; Yu, J. Titanium-rich TS-1 zeolite for highly efficient oxidative desulfurization. *Green Energy Environ***.** **2023**, 8, 163-172.
18. Soekiman, C.N.; Miyake, K.; Hayashi, Y.; Zhu, Y.; Ota, M.; Al-Jabri, H.; Inoue,R.; Y. Hirota, Y.; Uchida, Y.; Tanaka, S.; Kong, C.Y.; Nishiyama, N. Synthesis of titanium silicalite-1 (TS-1) zeolite with high content of Ti by a dry gel conversion method using amorphous TiO_2-SiO_2 composite with highly dispersed Ti species. *Mater. Today Chem*. **2020**, 16, 100209.
19. Petcu, G.; Anghel, E.M.; Somacescu, S.; Preda, S.; Culita, D.C.; Mocanu, S.; Ciobanu, M.; Parvulescu, V. Hierarchical Zeolite Y Containing Ti and Fe Oxides as Photocatalysts for Degradation of Amoxicillin. *J. Nanosci. Nanotechnol.* **2020**, 20, 1158–1169.

20. Petcu, G.; Dobrescu, G.; Atkinson, I.; Ciobanu, M; Blin, J.-L.; Parvulescu, V. Evolution of Morphology, Fractal Dimensions, and Structure of (Titanium) Aluminosilicate Gel during Synthesis of Zeolites Y and Ti-Y. *Fractal Fract.* **2022**, *6*, 663.
21. Zhao, Z.; Wang, N.; Zhang, H.; Shang, R.; Xing, J.; Zhang, D.; Li, J. Fabrication of ZSM-5 zeolite supported TiO_2-NiO heterojunction photocatalyst and research on its photocatalytic performance. *J. Solid State Chem.* **2022**, 309, 122895.
22. Badvi, K.; Javanbakht, V. Enhanced photocatalytic degradation of dye contaminants with TiO_2 immobilized on ZSM-5 zeolite modified with nickel nanoparticles. *J. Clean. Prod.* **2021**, 280, 124518.
23. Wang, C.; Shi, H.; Li, Y. Synthesis and characteristics of natural zeolite supported Fe^{3+}-TiO_2 Photocatalysts. *Appl. Surf. Sci.* **2011**, 257, 6873–6877.
24. Magdziarz, A.; Colmenares, J.C.; Chernyayeva, O.; Łomot, D.; Sobczak, K. Sonication and light irradiation as green energy sources simultaneously implemented in the synthesis of Pd-Fe- and Pt-Fe-doped TiO_2-based photocatalysts. *J. Mol. Catal. A: Chem.* **2016**, 425, 1–9.
25. Alizadeh, T.; Kadkhodayan, H.; Construction of Zeolite/Fe_2ZnTiO_6/graphene oxide multifunctional nanocomposite with high efficiency for photocatalytic removal of inorganic pollutants under visible irradiation. *J. Phys. Chem. Solids* **2022**, 171, 110997.
26. Castaneda-Juarez, M.; Martinez-Miranda, V.; Almazan-Sanchez, P.T.; Linares-Hernandez, I.; Santoyo-Tepole, F.; Vazquez-Mejia, G. Synthesis of TiO_2 catalysts doped with Cu, Fe, and Fe/Cu supported on clinoptilolite zeolite by an electrochemical-thermal method for the degradation of diclofenac by heterogeneous photocatalysis. *J. Photochem. Photobiol., A* **2019**, 380, 111834.
27. Wang, C.; Shi, H.; Li, Y. Synthesis and characterization of natural zeolite supported Cr-doped TiO2 photocatalysts. *Appl. Surf. Sci.* **2012**, 258, 4328–4333.
28. Torkian, N.; Bahrami, A.; Hosseini-Abari, A.; Momeni, M.M.; Abdolkarimi-Mahabadi, M.; Bayat, A.; Hajipour, P.; Rourani, H.A.; Abbasi, M. S.; Torkian, S.; Wen,Y.; Mehr, Y.M.; Hojjati-Najafabadi, A. Synthesis and characterization of Ag-ion-exchanged zeolite/TiO_2 nanocomposites for antibacterial applications and photocatalytic degradation of antibiotics. *Environ. Res.* **2022**, 207, 112157.
29. Kohsuke Mori, K.; Miura, Y.; Sayoko Shironita, S.; Yamashita, H. New Route for the Preparation of Pd and PdAu Nanoparticles Using Photoexcited Ti-Containing Zeolite as an Efficient Support Material and Investigation of Their Catalytic Properties. *Langmuir* **2009**, 25, 18, 11180–11187.
30. Petcu, G.; Papa, F.; Atkinson, I.; Baran, A.; Apostol, N.G.; Petrescu, S.; Richaudeau, L.; Blin, J.-L.; Parvulescu, V. Co- and Ni-Doped TiO_2 Nanoparticles Supported on Zeolite Y with Photocatalytic Properties. *Nanomaterials* **2023**, 13, 2200.
31. Qin, Z.; Wang, B.; Asano, N.; Wang, L.; Zhou, Y.; Liu, X.; Shen, B.; Mintova, S.; Asahina, S.; Valtchev, V. Towards a comprehensive understanding of mesoporosity in zeolite Y at the single particle level. *Inorg, Chem. Front*. **2022**, 9, 2365-2373.
32. Thommes, M.; Kaneko, K.; Neimark, A.V.; Olivier, J.P.; Rodriguez-Reinoso, F.; Rouquerol, J.; Sing, K.S.W. Physisorption of Gases, with Special Reference to the Evaluation of Surface Area and Pore Size Distribution (IUPAC Technical Report). *Pure Appl. Chem*. **2015**, 87, 1051–1069.
33. Hess, C. New advances in using Raman spectroscopy for the characterization of catalysts and catalytic reactions. *Chem. Soc. Rev*., **2021**, 50, 3519.
34. Yu, Y.; Xiong, G.; Li, C.; Xiao, F.S. Characterization of aluminosilicate zeolites by UV Raman spectroscopy. *Micropor. Mesopor. Mater.* **2001**, 46, 23-34.
35. Ilieva, L.; Petrova, P.; Venezia, A.M.; Anghel, E.M.; State, R.; Avdeev, G.; Tabakova, T. Mechanochemically Prepared Co_3O_4-CeO_2 Catalysts for Complete Benzene Oxidation. *Catalysts* **2021**, 11, 1316.
36. Wang, W.; Liu, Y.; Xua, C.; Zheng, C.; Wang, G. Synthesis of NiO nanorods by a novel simple precursor thermal decomposition approach. *Chem. Phys. Lett*. **2002**, 362, 119-122.
37. Mendoza-Castro, M.J.; De Oliveira-Jardim, E.; Ramírez-Marquez, N.-T.; Trujillo, C.-A.; Linares, N.; García-Martínez, J. Hierarchical Catalysts Prepared by Interzeolite Transformation, *J. Am. Chem. Soc*. **2022**, 144, 5163–5171.
38. Zhang, J.; Xu, Q.; Li, M.; Feng, Z.; Li, C. UV Raman Spectroscopic Study on TiO_2. II. Effect of Nanoparticle Size on the Outer/Inner Phase Transformations. *J. Phys. Chem. C* **2009**, 113, 1698–1704.
39. Bian, K.; Zhang, A.; Yang, H.; Fan, B.; Xu, S.; Guo, X.; Song, C. Synthesis and Characterization of Fe-Substituted ZSM-5 Zeolite and Its Catalytic Performance for Alkylation of Benzene with Dilute Ethylene. *Ind. Eng. Chem. Res*. **2020**, 59, 22413–22421.
40. Fan, F.; Feng, Z.; Li, C. UV Raman spectroscopic study on the synthesis mechanism and assembly of molecular sieves. *Chem. Soc. Rev*. **2010**, 39, 4794–4801.
41. Rana, B.S.; Singh, B.; Kumar, R.; Verma, D.; Bhunia, M.K.; Bhaumik, A.; Sinha, A.K. Hierarchical mesoporous Fe/ZSM-5 with tunable porosity for selective hydroxylation of benzene to phenol, *J. Mater. Chem*. **2010**, 20, 8575-8581.
42. https://www.thermofisher.com/ro/en/home/materials-science/learning-center/periodic-table/transition-metal/iron.html

43. https://www.thermofisher.com/ro/en/home/materials-science/learning-center/periodic-table/transition-metal/cobalt.html
44. https://www.thermofisher.com/ro/en/home/materials-science/learning-center/periodic-table/transition-metal/nickel.html
45. https://www.thermofisher.com/ro/en/home/materials-science/learning-center/periodic-table/transition-metal/titanium.html
46. Czuma, N.; Zarębska, K.; Motak,M.; Gálvez, M.E.; Da Costa, P. Ni/zeolite X derived from fly ash as catalysts for CO_2 methanation. *Fuel* **2020**, 267, 11713.
47. Alalga, L.; Benamar, A.; Trari, M. Hydrogen production via methane decomposition over nickel supported on synthesized ZSM-5/MCM41 zeolite composite material, *Int. J. Hydrog. Energy*. **2021**, 46, 28501-28512.
48. Ren, T.; Shiyao,W.; Chen-shuai, L.; Xu, W.; Xia, A.; Xian-mei, X. Synthesis of the hierarchical Fe-substituted porous HBeta zeolite and the exploration of its catalytic performance, *J. Fuel Chem. Technol*. **2019**, 47, 1476-1485.
49. Zhang, T.; Qiu, Y.; Liu, G.; Chen, J.; Peng, Y.; Liu, B.; Li, J. Nature of active Fe species and reaction mechanism over high-efficiency Fe/CHA catalysts in catalytic decomposition of N_2O. *J. Catal*. **2020**, 392, 322-335.
50. Xin-yu, P.; Li-jun, L.; Bo-xiong, S.; Yao, B.; Li-chao, S. Insight into the catalytic oxidation of toluene over M/ZSM-5 (M=Cu, Mn, Fe, Ce, Ti) catalysts. *J. Fuel Chem. Technol*. 2023, 51, 841−851.
51. Lebedeva, O.E.; Wolfgang M. H. Sachtler, W. M.H. Enhanced Reduction of Fe_2O_3 Caused by Migration of TM Ions out of Zeolite Channels. *J. Catal*. **2000**,191, 364–372.
52. Rabee, A.I.M.; Gaid, C.B.A.; Mekhemer, G.A.H.; Zaki, M.I. Combined TPR, XRD, and FTIR studies on the reduction behavior of Co_3O_4. *Mater. Chem. Phys.* **2022**, 289, 126367.
53. Xue, C.; Xue-feng, W.; Xun, W.; Cun-bao, D.; Min-min, C. Effect of highly dispersed Co_3O_4 on the catalytic performance of $LaCoO_3$ perovskite in the combustion of lean methane. *J. Fuel Chem. Technol.* **2023**, 51, 367−375.
54. Wang , Y.; Wang, H.; Shao, Y.; Li, T.; Tatsumi, T.; Wang, J.-G. Direct Synthesis of Ti-Containing CFI-Type Extra-Large-Pore Zeolites in the Presence of Fluorides. *Catalysts* **2019**, 9, 257.
55. Tang, B.; Dai, W.; Sun, X.; Guan,N.; Li, L.; Hunger, M. A procedure for the preparation of Ti-Beta zeolitesfor catalytic epoxidation with hydrogen peroxide. *Green Chem*. **2014**, 16, 2281.
56. Saramok, M.; Szymaszek, A.; Inger, M.; Antoniak-Jurak, K.; Samojeden, B.; Motak, M. Modified Zeolite Catalyst for a NOx Selective Catalytic Reduction Process in Nitric Acid Plants. *Catalysts* **2021**, 11, 450.
57. Bhargava, R.; Khana, S.; Ahmad, N.; Ansari, M.M.N. Investigation of Structural, Optical and Electrical Properties of Co3O4 Nanoparticles, *2nd International Conference on Condensed Matter and Applied Physics (ICC 2017)* AIP Conf. Proc. 1953, 030034-1–030034-4; https://doi.org/10.1063/1.5032369
58. Emayavaramban, P.; Babu, S. Ganesh; Karvembu, R.; Dharmaraj, N. Nickel Oxide Doped Hydroxyapatite for Catalytic Oxidation of Alcohols to Carbonyl Compounds at Room Temperature**.** *Adv. Sci. Eng. Med.* **2014**, 6, 659-666(8).
59. Gingasu, D.; Oprea, O.; Marinescu, G.; Calderon Moreno, J.M.; Culita, D.C.; Preda, S.; Surdu, V.-A. Structural, Morphological, and Optical Properties of Single and Mixed Ni-Co Aluminates Nanoparticles. *Inorganics* **2023**, 11, 371.
60. Mannaa, M.A.; Qasim, K.F.; Alshorifi, F.T.; El-Bahy, S.M.; Salama, R.S.Role of NiO Nanoparticles in Enhancing Structure Properties of TiO2 and Its Applications in Photodegradation and Hydrogen Evolution. *ACS Omega* **2021**, 6, 30386−30400.
61. Jiang, D.; Otitoju, T.A.; Ouyang, Y.; Shoparwe, N.F.; Wang, S.; Zhang, A.; Li, S. A Review on Metal Ions Modified TiO_2 for Photocatalytic Degradation of Organic Pollutants. *Catalysts* **2021**, 11, 1039.
62. Saha, A.; Moya, A.; Kahnt, A.; Iglesias, D.; Marchesan, S.; Wannemacher,R.; Prato, M.;. Vilatela, J.J.; Guldi, D.M. Interfacial charge transfer in functionalized multiwalled carbon nanotube@TiO_2 nanofibres. *Nanoscale* **2017**, 8(00), 1-3.
63. Negoescu, D.; Atkinson, I.; Gherendi, M.; Culita, D.C.; Baran, A.; Petrescu, S.; Trica, B.; Ionescu, R.; Pelinescu, D.; Bratan, V.; Parvulescu, V. Brij 58–activated carbon assisted synthesis of Ag/Ag_2O/TiO_2-AC photocatalysts for efficient organic pollutants degradation, *J. Alloys Comp*. **2023**, 931, 167528.
64. Hassan, S. M.; Ahmed, A. I.; Mannaa, M. A. Surface Acidity, Catalytic and Photocatalytic Activities of New Type $H_3PW_{12}O_{40}$/Sn-TiO_2 Nanoparticles. *Colloid. Surface. Physicochem. Eng. Aspect.* **2019**, 577, 147−157.
65. Li, D.; Cheng, X.; Yu, X.; Xing, Z. Preparation and Characterization of TiO_2-Based Nanosheets for Photocatalytic Degradation of Acetylsalicylic Acid: Influence of Calcination Temperature. *Chem. Eng. J.* **2015**, 279, 994−1003.
66. Zhou, M.; Yu, J.; Liu, S.; Zhai, P.; Jiang, L. Effects of Calcination Temperatures on Photocatalytic Activity of SnO_2/TiO_2 Composite Films Prepared by an EPD Method. *J. Hazard. Mater*. **2008**, 154, 1141−1148.
67. Liqiang, J.; Yichun, Q.; Baiqi, W.; Shudan, L.; Baojiang, J.; Libin, Y.; Wei, F.; Honggang, F.; Jiazhong, S. Review of photoluminescence performance of nano-sized semiconductor materials and its relationships with photocatalytic activity. *Sol. Energy Mater Sol. Cells* **2006,** 90, 1773–1787.

68. Liang, W.; Xu, G.; Fu, Y. Selective photocatalytic oxidation of furfural to C4 compounds with metal-TS-1 zeolite. *Appl. Catal. B*. **2024**, 340 123220.
69. Saeed, M.; Usman, M.; Ibrahim, M.; Haq, A.; Khan,I.; Ijaz, H.; Akram, F. Enhanced photo catalytic degradation of methyl orange using p–n Co_3O_4-TiO_2 heterojunction as catalyst. *Int. J. Chem. React. Eng*. **2020**, 18, 20200004.
70. Lizeth Katherine, T.N.; Vendula, B.; Jaroslav, K.; Jaroslav, C. Structure and Photocatalytic Properties of Ni-, Co-, Cu-, and Fe-Doped TiO_2 Aerogels. *Gel* **2023**, 9, 357.
71. Din, S.T.U.; Xie, W.-F.; Yang, W. Synthesis of Co_3O_4 Nanoparticles-Decorated $Bi_{12}O_{17}Cl_2$ Hierarchical Microspheres for Enhanced Photocatalytic Degradation of RhB and BPA. *Int. J. Mol. Sci.* **2022**, 23, 15028.
72. Tang, J; Fu, M.; Mao, Y.; Yang, S.; Lin, W.; Yu, Y.; Song, S. Decorating {0 0 1} TiO_2 nanosheets on hydrophobic NaY zeolite: An efficient deactivation-resistant photocatalyst for gaseous toluene removal. *Chem. Eng. J.* **2023**, 472, 144883.
73. Teodorescu, C.M., Esteva, J.M.; Karnatak, R.C.; El Afif. A. *Nucl. Instrum. Meth. Phys. Res. A* **1994**, 345, 141-1.